Piezo-phototronic Effect Enhanced Photodetector Based on MAPbI₃ Perovskite

Jiaheng Nie [1,2], Yan Zhang [1,3,4,*], Lijie Li [5,*], and Jizheng Wang [2,*]

[1] *School of Physics, University of Electronic Science and Technology of China, Chengdu 610054, China*

[2] *Chinese Acad Sci, Inst Chem, Beijing Natl Lab Mol Sci, CAS Key Lab Organ Solids, Beijing 100190, China.*

[3] *Beijing Institute of Nanoenergy and Nanosystems, Chinese Academy of Sciences, Beijing 100083, China*

[4] *College of Nanoscience and Technology, University of Chinese Academy of Sciences, Beijing 100049, China*

[5] *Multidisciplinary Nanotechnology Centre, College of Engineering, Swansea University, Swansea, SA1 8EN, UK*

[*] To whom correspondence should be addressed, E-mail: zhangyan@uestc.edu.cn, L.Li@swansea.ac.uk and jizheng@iccas.ac.cn

Abstract

Recent research on the hybrid organic-inorganic perovskites has greatly advanced the fields of photovoltaics, photodetection, and light emission. Emerging of piezotronics and piezo-phototronics has led to tremendous high-performance devices that are based on piezoelectric materials. Although many previous researches were centered around the single crystal hybrid perovskites, polycrystalline materials are easier to fabricate such as using the solution-process, and have many other advantages, e.g. low cost, low environmental requirements, and high conversion efficiency. So far there are very few reports of piezotronically modulated polycrystalline perovskite devices. Here, a novel piezo-phototronic effect enhanced photodetector based on MAPbI₃ polycrystalline perovskite is designed, fabricated, and subsequently characterized. With polycrystalline materials, it is seen that the device

performances can be significantly enhanced using the piezo-phototronic effect. Moreover the polycrystalline perovskites introduce unprecedented potentials to fine tune the devices from weak to strong piezoelectric performance. Our study explores the possibility of using polycrystalline perovskites to create high performance strain-controlled piezo-phototronic devices, which will have promising applications in internet of things, multifunctional micro/nanoelectromechanical devices and sensor networks.

Keywords: Piezo-phototronics, Perovskite, Schottky barrier, Polycrystalline MAPbI3, Strain.

1. Introduction

Coupling semiconducting properties, piezoelectric effect, and photoexcitation, piezotronics and piezo-phototronics[1-6] have attracted extensive attention especially in energy harvesting,[7-9] self-powered systems,[10, 11] nanogenerators,[12-14] and biomedicine field.[4, 15-17] The fundamental principle of piezo-phototronics has been reported that the energy band structure at the contact can be tuned by strain-induced polarization charges, as a result, the photoelectric process is controlled by the mechanical stimulation.[18] The piezo-phototronic effect has been reported to enhance the performance of the photodetectors, solar cells with ZnO-CdS Double-Shell microwire,[19] and MoS_2 materials.[20, 21] A piezo-multifunctional structure of $Li_xNbO_3:Pr^{3+}$ was reported to have a high piezo-luminescence intensity far exceeding other well-known structures.[22] Piezo-phototronic devices show exceptional superiority in light-emitting diodes (LEDs),[18] logical devices,[23-25] solar cells,[26, 27] strain gated vertical nanowire arrays,[28] and ultrahigh-performance sensors.[29-32] The transport, separation, and recombination processes of carriers are controlled by strain-induced polarization charges in those devices.

Recently, strain-tunable perovskite photodetectors based on the $MAPbI_3$ single crystal have been intensively studied, and the principle of photocurrent controlled by strain has been discussed.[33] A $MAPbI_3$ solar cell based on the piezo-phototronic effect has been fabricated to improve the power conversion efficiencies (PCE) by 40%.[34] Depending on excellent properties

of high absorption coefficient,[35, 36] long charge carrier lifetime[37, 38] long diffusion length,[39, 40] high carriers mobility,[41, 42] and high piezoelectric coefficient,[43] organic-inorganic hybrid perovskites have been significantly attracting broad research interests.

Piezoelectric perovskite materials with organic-inorganic lead halide have attracted more and more attentions, especially in the field of optoelectronics.[43] The d_{33} of perovskite has been proven by the direct optical testing, which is 2.7 pm/V in $CH_3NH_3PbI_3$ single crystal and 6 pm/V in polycrystalline film via the measurement of PFM (piezoresponse force microscopy).[44, 45] The piezoresponse of the lead-halide perovskite has been investigated by PFM to exhibit polarization properties Ps =13 $\mu C/cm^2$.[46] Related study of the $MAPbI_3$ polarization by density functional theory and symmetry mode analysis has been reported.[47] The piezoelectric properties of perovskites are used to control or tune the performance of photodetector devices, and offer novel methods to improve the performance of photodetector devices, which is known as piezotronic and piezo-phototronic effects on perovskites.[33]

Perovskites can be prepared on a large scale by the solution engineering,[48, 49] printing method,[50-52] and vapor–solution.[53] It exhibits excellent coupling characteristics among the photovoltaic properties,[54] semiconductor properties, and piezo-phototronics.[33] Fabricated solar cells and photodetectors devices are superior candidates for future optoelectronic devices. Photodetectors based on perovskites converting visible optical signals to electrical signals instantaneously, have various potentials in high performance sensing,[55, 56] image processing,[57] and optical communication.[58] Hybrid perovskite single-crystal photodetectors have been reported to demonstrate a very narrow spectral response, with a full-width at half-maximum of <20 nm.[59] So far, apart from the majority of photodetectors that use vertical heterojunctions, photodetectors using planar structures have greater advantages for planar photodetectors array and image processing.[19, 60] Three-dimensional vertical perovskite nanowires array has been designed to achieve high-performance optoelectronic devices.[61] Meanwhile, solar cell devices made from perovskite materials have been attracting more attention, and its current efficiency has reached to 25.2%.[62] Stability of $MAPbI_3$ solar cell is reported to be >1000 hours, by using double layer of mesoporous TiO_2 and ZrO_2 as a scaffold infiltrated.[63]

The main feature of Schottky-diode based photodetectors is the metal–semiconductor contacts. The barrier height at the contact can be predicted by the Schottky–Mott rule on the

basis of the relative alignment of energy levels in the ideal case. Metal–semiconductor contacts, known as the Schottky barrier, are at the core of current electronics, optoelectronics, and integrated circuits.[64, 65] One of the most significant parameters of the metal-semiconductor contact is the Schottky barrier height (Φ_{SB}). The Schottky barrier height means an energy barrier for charge carriers (Electron or Hole) to pass through the contact, which can essentially characterize the efficiency of charge transport and performance of the whole device. When applying strain, the polarized charge causes piezoelectric potential in the contact region, resulting in unbalanced carrier distributions. As a result, the energy band at both ends of the device appears asymmetric. This mechanism causes different changes in the Schottky potential on both sides. The piezoelectric polarization caused by strains in a pseudo-semiconductor heterostructure can change the electronic and optoelectronic properties of the semiconductor, such as the spectral response of the light modulator and the threshold voltage of the electron-field effect transistor. The barrier height under the applied stress changes; and the free charge carrier density neutralizes strain-induced polarization charges in the semiconductor-metal interface affecting the Fermi level relative to the edge of the surface contact conduction band.

In this paper, a new photodetector based on MAPbI$_3$ polycrystalline is designed in response to the changes of light intensity and mechanical strain. Controllable strain changes the distribution of polarized electric field by polarized charges. Strain, as a mechanical stimulation, enhances the separation process of electron-hole pairs and hinders the electron-hole recombination process, regulating the positive and negative charges distribution at the interface of the contact. Thus, the strain-induced piezoelectric field causes an asymmetric change of the Schottky barriers and energy levels. While the strain causes negative charges building-up at the contact interface, the Schottky barrier rises, and the current decreases. The opposite situation causes the Schottky barrier to move down and the current increases. In this work, the mechanism of strain controlled Schottky barriers in organic-inorganic hybrid perovskite (MAPbI$_3$) polycrystalline devices have been investigated, which provides a fundamental model for the future human-computer interaction, multi-functional micro-nano system.

2.   Results and discussion

The experimental process of the perovskite photodetector includes the preparation of the

perovskite layer, the array plating process, and the experimental measurement, which are shown in Figure 1. The prepared 1 mol/L MAPbI$_3$ solution in Figure 1a, was made by mixing 1:1 with MAI and PbI$_2$, and the solvent was DMF mixed DMSO at a ratio of 9:1. Subsequently, MAPbI$_3$ solution was placed on a mixing table at a temperature of 60 °C for two hours. The process of perovskite depositing on PET was done using the one-step spin coating method. The rotation speed started slow and then became faster for 40 seconds. During this time, chlorobenzene is added as anti-solvent as shown in Figure 1b. Figure 1c shows the annealing process. For solution treated perovskites, the formation of perovskites may occur in the temperature range of 40-160 °C.[66] It has been reported that MAPbI$_3$ is annealed at 100 °C to form a uniform black film with a stable absorption profile because the time required for complete conversion of the perovskite film is effectively reduced at annealing process.[67] In order to obtain a perovskite photodetectors array, we used a shadow mask on the surface of the perovskite during the electrode plating process so that Au can be deposited according to the predetermined structure, as shown in Figure 1d. The jagged channel of the unit between the two electrodes is very narrow and more efficient than parallel channels. The digital image of the prepared photodetectors array is shown in the Figure 1e, showing Au (higher stability than other metals on perovskite) was electroplated onto a PET or flexible substrate (polyimide) in a 4 x 5 matrix structure by a coater. In addition to the PET, the photodetectors array can also be deposited onto a polyimide film. In our study, we fabricated the device by spin-coating perovskite polycrystalline films onto PET substrate, which is bent to produce the tensile strain. For the positive polarization case, the tensile strain induces positive polarization charges, which decrease the potential barrier height. For the negative polarization case, the tensile strain induces negative polarization charges, which increase the potential barrier height. Keithley 4200 is used to measure the electrical characteristics, which is connected to the device with probes. In the dark environment, the influence of external light is excluded, and a beam of light is introduced from the microscope to the detector device. The I-V characteristic of the photodetector was tested under a microscope with various strains. Figure 1f shows a deformation generator, and the device is bent due to the displacement of the baffle. The value of the strain is calculated by the formula shown in Figure 1f. Initially, the PET substrate with photodetectors array was placed horizontally without strain. Then, the PET substrate is slowly stressed, and the center of the PET substrate is lifted upward.

Since PET has a thickness, the MAPbI$_3$ film on the upper surface of the substrate is stretched by the surface. The length of the PET substrate is L bent by the displacement actuator, and the length change of the PET substrate is Δx under the horizontal stress. The slope θ is consistent with changes of the baffle displacement of the displacement actuator.

Organic-inorganic hybrid Lead-containing perovskites have common general formula $C_nH_{2n+1}NH_3PbX_3$, mainly consisting of these two structures: the tetragonal perovskite $CH_3NH_3PbI_3$ and the orthorhombic perovskite $CH_3NH_3PbI_3$. The skeleton consists of Pb and I, whose unit is a cage surrounded by PbI_6, and $CH_3NH_3^+$ moves conditionally in the skeleton. Figure 2a shows the two crystal structures of perovskites. XRD pattern of the MAPbI$_3$ at room temperature is shown in Figure 2b. By using the scanning electron microscopy (SEM), the top view SEM image is shown in Figure 2c, demonstrating a completely covered perovskite film structure. The absorption spectra demonstrate the absorption range of ~350 - 900 nm, and the peak is near at 500nm, as shown in Figure 2d. In the XRD pattern, we observe two characteristic perovskite peaks near 14°, 28° (2θ), corresponding to (110), (220) crystal directions. Extremely low peaks in other directions indicate that the intensity of the intermediate phases is weak.

We have studied the photocurrent-voltage characteristics of the MAPbI$_3$ photodetector at various strains or different illumination power densities in Figures 3a & 3b. The optical white light illumination source uses XZ-105WA Halogen lamp to conduct the characterization of the photodetector with wavelength range of ~ 400-800 nm to mimic the irradiation of the sun light. The photocurrent presents 253 nA, 248 nA, 108 nA, and 99 nA with fixed bias voltage of 10 V, forming a decreasing trajectory with strain range from 0%, 1.4%, 3.4% to 4.7%, as the power density fixed at 31.7 $\mu W/cm^2$, which is shown in Figure 3a. The I−V characteristics at fixed strain valued 1.4% with the power density range from 6.6 $\mu W/cm^2$, 16.5 $\mu W/cm^2$, 31.7 $\mu W/cm^2$ to 84.6 $\mu W/cm^2$ have been presented in Figure 3b. When the strain is 1.4%, the device displays photocurrents of 120 nA, 248 nA, 389 nA, and 586 nA, at the fixed bias voltage of 10 V. Experimental observations show that the illumination is positively correlated with the current. The increasing strain causes the I-V curve to become flattened, indicating that the Schottky barrier is enhanced by the strain and the device conductance decreases with the strain. Figure 3d shows that the photocurrent decreases with the strain, describing the effect of polarized charges due to strains with various power densities. In the strain range of 1.5% to 3%, the curves

have larger slopes. For the polymorphic perovskite structure, the polar directions of the crystals are different due to the random distribution of asymmetric structures. The polar direction, which accounts for the majority of the ratio, controls the polarity of the entire structure. For the Schottky contact, positive charges on the surface will change the energy band and decrease the Schottky barrier height. The existence of ferroelectric domains, electrochemical phenomena, ion migration, electrostatic effects, and other factors, will reduce the piezotronic effect on MAPbI$_3$ polycrystalline.

The cross-sectional view of the photodetector shows a sandwiched structure of PET/perovskite/Au, as shown in Figure 4a. Perovskite layer is stacked by the interdiffusion of lead iodide (PbI$_2$) solution and methyl ammonium halide (MAI) solution by spin-coating. Then, according to the predetermined shape, the parallel electrode is plated on the upper surface of the perovskite. When a beam of light incidents on the top surface, free carriers inside MAPbI$_3$ are generated. Most photogenerated excitons are dissociated into free charges in the perovskite layer, and the electrodes can effectively collect free charges even without electron or hole receiving layers. In the case of presence of an applied voltage, carriers (electron-hole pairs) are excited by light and subsequently separated. There are defects generated in the crystal during the poling process. The intense local piezoelectric effect is exhibited in organometallic trihalide perovskite (OTP) polycrystals due to grain boundaries caused by the piezoelectric polarization induced by polycrystalline ion migration.[44] When the bias voltage is applied at both ends, the drift of the electron and hole pairs is accelerated, and the electrons and holes are caused to accumulate near the positive and negative metal-semiconductor contacts. At this time, the third factor, strain, as the external control condition, regulates the strain-induced polarization charges inside the metal semiconductor, and regulates the Schottky barrier of the metal semiconductor interface by the piezoelectric potential caused by the polarization charge.[57] Figure 4b displays the poling electric field distribution on the top surface, which is a nonuniform electric field induced by lateral-structured electrodes leading to polarized charge displacements under applied voltages. The polarization charges accumulate at both ends to form a narrow piezoelectric potential region. Under the strain and illumination, electric field, the drift of carriers, separation of electron-hole pairs, and recombination processes are regulated, and the electrical current changes. The regulation of the strain on the device can be classified into two

aspects. The negative polarization charges promote the drift of the electrons to the Metal-Semiconductor contact, the Schottky barrier of the metal semiconductor interface increases, so the photocurrent decreases (Figure 4e). The positive polarization charges promote the free electron to drift away from the barrier, and the Schottky barrier height of the metal-semiconductor interface decreases, therefore the photocurrent increases, as show in Figure 4f. The height of the Schottky barrier on both sides shows a similar change, which increase (decrease) the corresponding SBHs of local contacts. Figure 4e and 4f demonstrate changes in the Schottky barrier of the metal-semiconductor interface induced by applied strains.

Alongside the study of electric field and light effect, we introduce strain as the third variable quantity. The piezotronic properties of MAPbI$_3$ crystal have been experimentally proved. Piezoelectric properties are directly related to the displacement of ions at different lattice positions. MAPbI$_3$ single crystal show a strong piezoelectric behavior after piezoelectric poling along [001] direction, and rectification property can be improved.[44] Strain-induced piezoelectric charges can significantly enhance the performance in photodetector device based on MAPbI$_3$ single crystal.[33] For the prepared polymorphic MAPbI$_3$ crystal, due to lattice polarities in different directions. The direction of the piezoelectric electric field generated by the strain will also be random. The piezoelectric induced electric field of the same direction as the applied electric field will reduce the energy band of the contact region, while the opposite behavior will increase the energy band of the contact region. The band change induced by strain is indicated by a dotted line in Figures 4c and 4d. The effect of piezoelectric polarization on SBH is due to polarization generated charges at the metal-semiconductor interface, thereby changing the local Fermi level and adjusting the local conduction band distributions.

If the polarization directions of most charges tend to be uniform, the overall piezoelectric properties are clearly observed. Strain-induced SBH change affects the electric characteristics of the contact. Figures 5a and 5b displays the positive effect of strain on polarized charges. The photocurrent induced by the power density of 6.6 μW/cm^2 increases with the increase of the tensile strain. When the tensile strain increases to 1.4%, the photocurrent under 10 V bias voltage rises from 4 to 5 nA. When the tensile strain further increases from 1.4% to 3.4%, the photocurrent increases to 13 nA. The current induced by 3.4% is 2.6 times higher than the current with strain of 1.4%. When the tensile strain further increases from 3.4% to 4.7%, the

photocurrent increases to 16 nA. The photocurrent under the power density of 6.6 µW/cm^2 as a function of the bias voltage under different tensile strains is shown in Figure 5a. The light-induced photocurrent as a function of strain is displayed in Figure 5b with bias voltages of 2.5 V, 5.0 V, 7.5 V, and 10 V, describing the relationship between photocurrent and strain. It is found that the photocurrent at 10 V bias monotonously increases with the applied tensile strain. At the same time, polycrystalline material devices seldom change by strain, as shown in Figures 5c and 5d. This is due to polarized charges interacting with each other in the device. In our non-polarization devices, the changes of current-voltage characteristics show that the performance of the device is independent of polarization. This case can be considered as strain independent. The resistance of perovskite polycrystalline films changes by strain, indicating that the piezoresistance effect plays a priority role. The piezoresistance type device has linearly symmetric I-V photoelectric behavior. The piezo-phototronic devices have nonlinear current-voltage characteristics. The measurements in Figure 5 imply that the polycrystalline perovskites have great advantages of generating devices that have much greater piezotronic effects, as well as strain-free devices that have applications in certain areas.

According to previous works, D. Pesquera et al. have shown the effects of symmetry breaking (strain ranging from 0.3% to 0.9%), indicating that the strain can tune the ($3z^2$-r^2/x^2-y^2) occupancy ratio and the metal–oxygen bond lengths of oxides.[68] V. Laukhin et al. reported that strain-driven structural transformations lead to electronic subband reconfiguration in a d^0-Perovskite.[69] The change of morphology and structure changes of perovskite leads to the various changes in material properties, such as polarization, ferroelectricity property,[70] ionic properties,[71] lattice parameter,[72] and charge transfer kinetics of the electrode interface.[73] In our study, the strain also change the morphology and structure changes of perovskite polycrystals. However, the polarization charges play an important role for current-voltage characteristics of our piezo-phototronic polycrystalline perovskite photodetectors. The morphology and structure changes by strain are neglected in our works. Because the devices have same materials and structure, which are applied tensile strain under the same conditions. In our experiments, there are three cases: positive polarization charge case (Figure 5a), the negative polarization charge case (Figure 3a), and non-polarization charge case (Figure 5c), respectively.

The photoresponsivity R is given by,[33]

$$R = \frac{I_{light} - I_{dark}}{P_{ill}} = \frac{I_{light} - I_{dark}}{I_{ill} \times S}$$ (1)

where, I_{light}, I_{dark}, and I_{ill} are the photocurrent, dark current and excitation power density, respectively. S is the effective light area, and P_{ill} is the illumination power. Thus, its relative change Δ, is calculated by[33]

$$\Delta = \left| \frac{\Delta R}{R} \right| = \left| \frac{R - R_0}{R_0} \right|$$ (2)

Figures 6a and 6b illustrate the change of photoresponsivity by the positive and negative polarization charges, respectively. The positive polarization charges promote the improvement of photoresponsivity with the strain, under various bias voltages at the power density of 6.6 μW/cm^2, while the negative polarization charges show a decreasing trend with the strain at the power density of 31.7 μW/cm^2. In Figure 6c, $\Delta R/R$ increases with the strain at higher bias voltage of 10 V. Under lower bias voltage, $\Delta R/R$ has a minimum value with various strains from 0% to 4.7%. Figure 6d shows the opposite trend by strain-induced negative polarization charges. These results indicate that applied strain can effectively modulate the sensitivity of photodetector.

Figure 7 illustrates response time versus strain under positive and negative polarization charges at the illumination power density of 31.7 μW/cm^2 with a bias voltage of 10 V. The response time has a similar tendency with photoresponsivity induced by strain. At the negative polarization charges case, the response time increases from 0.809 s to 1.114 s with strain from 0% to 4.7%. While the response time decreases from 0.947 s to 0.587 s, under positive polarization charges case. Figure 7c shows that the response time decrease with strain in the positive polarization charges case. In the negative polarization charges case, the response time increase with strain. Thus, the response time of device based on MAPbI$_3$ polycrystalline films can be obviously affected by strain.

Piezo-phototronic effect tuning the device performance under the mechanical strain has novel applications in high-resolution strain mapping, high-sensitivity smart sensing devices, and micro/nano optoelectronic-mechanical systems. For example, a high-resolution

electroluminescent imaging device was fabricated by composing n-ZnO nanowire/p-GaN light-emitting diode array to produce a pressure map under a compressive strain.[74] InGaN/GaN multiple quantum wells based high-resolution dynamic tactile/pressure displays were reported to have a 6350 dpi pixel density for linearly strain (0% - 0.15%).[75] A n-ZnO/p-SnS core-shell NW array solar cell can be effectively enhanced by bending the structure of solar cell devices.[26] Chen et al. have explored a ZnO-Ga$_2$O$_3$ core-shell heterojunction microwire that is highly sensitive to UV light.[76] The sensitivity of the strain-controlled photodetector under the -0.042% strain achieved three times higher than that of no strain.[76]

3.   Conclusion

In summary, an array of photodetectors based on organic-inorganic hybrid perovskite (MAPbI$_3$) regulated by strains has been demonstrated. The effects of light, voltage, and strain on the photodetector have been thoroughly investigated through systematic experimentations. The change in photocurrent caused by strains is further explored. The photodetector based on MAPbI$_3$ perovskite on a flexible substrate can be regulated by strains, as the Schottky barrier of the Au-MAPbI$_3$ contact is profoundly affected by the strain, and the electric field formed by the polarization charges caused by the strain tunes the transport, separation, and recombination of the carriers. This work provides a novel investigation on polycrystalline perovskite strain-modulated photo detecting mechanism, which will have much greater practicality than single crystalline perovskite devices.

4.   Experimental Method

4.1 Device Fabrication:

The PET (thickness of ~1mm) was cleaned in turn by deionized water, and ethanol about 45 mins respectively, and cleaned PET substrates are put in the plasma generator equipment to produce rough surfaces, facilitating the spin coating process of the solution. Then, a layer of MAPbI$_3$ film was grown by the spin-coating method. The MAPbI$_3$ precursor which compounded PbI$_2$ and Methylammonium iodide (CH$_3$NH$_3$I) with a density of 1M, was dissolved in organic mixed solution (DMF 90%, DMSO 10%) at 60°C temperature with ~2h mixing process. After spin-coating, the system was annealed by a hot stage for ~10 min at

100 °C and then cooled to room temperature naturally, and chlorobenzene is added during the period. After that, the Au electrode layer is electroplated on the top surface of $MAPbI_3$ layer by DC magnetron sputtering at room temperature.

4.2 Characterization:

We perform I-V tests using the setup composed of Keithley 4200 and Micromanipulator 6150 probe station at room temperature and the ambient air pressure. The optical source is the white light from the Z-105WA Halogen lamp. Absorption spectra were quantified using the JASCO V-570 spectrophotometer.

Competing interests

The authors declare no competing interests.

References

1. Wang, Z. L.; Wu, W., Piezotronics and piezo-phototronics: fundamentals and applications. *National Science Review* **2014,** *1* (1), 62-90.

2. Wang, Z. L., Nanogenerators, self-powered systems, blue energy, piezotronics and piezo-phototronics – A recall on the original thoughts for coining these fields. *Nano Energy* **2018,** *54,* 477-483.

3. Zhang, Y.; Leng, Y.; Willatzen, M.; Huang, B., Theory of piezotronics and piezo-phototronics. *MRS Bull.* **2018,** *43* (12), 928-935.

4. Wang, Z. L.; Wu, W.; Falconi, C., Piezotronics and piezo-phototronics with third-generation semiconductors. *MRS Bull.* **2018,** *43* (12), 922-927.

5. Hao, J.; Xu, C.-N., Piezophotonics: From fundamentals and materials to applications. *MRS Bull.* **2018,** *43* (12), 965-969.

6. Bao, R.; Hu, Y.; Yang, Q.; Pan, C., Piezo-phototronic effect on optoelectronic nanodevices. *MRS Bull.* **2018,** *43* (12), 952-958.

7. Yang, X.; Xu, L.; Lin, P.; Zhong, W.; Bai, Y.; Luo, J.; Chen, J.; Wang, Z. L., Macroscopic self-assembly network of encapsulated high-performance triboelectric nanogenerators for water wave energy harvesting. *Nano Energy* **2019,** *60,* 404-412.

8. Lei, R.; Zhai, H.; Nie, J.; Zhong, W.; Bai, Y.; Liang, X.; Xu, L.; Jiang, T.; Chen, X.; Wang, Z. L., Butterfly-Inspired Triboelectric Nanogenerators with Spring-Assisted Linkage Structure for Water Wave Energy Harvesting. *Advanced Materials Technologies* **2019,** *4* (3).

9. Wang, J.; Pan, L.; Guo, H.; Zhang, B.; Zhang, R.; Wu, Z.; Wu, C.; Yang, L.; Liao, R.; Wang, Z. L., Rational Structure Optimized Hybrid Nanogenerator for Highly Efficient Water Wave Energy Harvesting. *Advanced Energy Materials* **2019,** *9* (8).

10. Luo, J.; Wang, Z. L., Recent advances in triboelectric nanogenerator based self-charging power systems. *Energy Storage Materials* **2019**.

11. Guo, H.; Pu, X.; Chen, J.; Meng, Y.; Yeh, M.-H.; Liu, G.; Tang, Q.; Chen, B.; Liu, D.; Qi, S.; Wu, C.; Hu, C.; Wang, J.; Wang, Z. L., A highly sensitive, self-powered triboelectric auditory sensor for social robotics and hearing aids. *Science Robotics* **2018,** *3* (20).

12. Wu, C.; Wang, A. C.; Ding, W.; Guo, H.; Wang, Z. L., Triboelectric Nanogenerator: A Foundation of the Energy for the New Era. *Advanced Energy Materials* **2019,** *9* (1).

13. Askari, H.; Khajepour, A.; Khamesee, M. B.; Saadatnia, Z.; Wang, Z. L., Piezoelectric and triboelectric nanogenerators: Trends and impacts. *Nano Today* **2018,** *22,* 10-13.

14. Bernier, M. C.; Li, A.; Winalski, L.; Zi, Y.; Li, Y.; Caillet, C.; Newton, P.; Wang, Z. L.; Fernandez, F. M., Triboelectric Nanogenerator (TENG) Mass Spectrometry of Falsified Antimalarials. *Rapid Commun. Mass Spectrom.* **2018**.

15. Ouyang, H.; Liu, Z.; Li, N.; Shi, B.; Zou, Y.; Xie, F.; Ma, Y.; Li, Z.; Li, H.; Zheng, Q.; Qu, X.; Fan, Y.; Wang, Z. L.; Zhang, H.; Li, Z., Symbiotic cardiac pacemaker. *Nat Commun* **2019,** *10* (1), 1821.

16. Liu, Z.; Nie, J.; Miao, B.; Li, J.; Cui, Y.; Wang, S.; Zhang, X.; Zhao, G.; Deng, Y.; Wu, Y.; Li, Z.; Li, L.; Wang, Z. L., Self-Powered Intracellular Drug Delivery by a Biomechanical Energy-Driven Triboelectric Nanogenerator. *Adv. Mater.* **2019,** *31* (12), e1807795.

17. Zhao, G.; Zhang, Y.; Shi, N.; Liu, Z.; Zhang, X.; Wu, M.; Pan, C.; Liu, H.; Li, L.; Wang, Z. L., Transparent and stretchable triboelectric nanogenerator for self-powered tactile sensing. *Nano Energy* **2019,** *59,* 302-310.

18. Zhang, Y.; Wang, Z. L., Theory of piezo-phototronics for light-emitting diodes. *Adv. Mater.* **2012,** *24* (34), 4712-8.

19. Zhang, F.; Niu, S.; Guo, W.; Zhu, G.; Liu, Y.; Zhang, X.; Wang, Z. L., Piezo-phototronic Effect Enhanced Visible/UV Photodetector of a Carbon-Fiber/ZnO-CdS Double-Shell Microwire. *ACS Nano* **2013,** *7* (5), 4537-4544.

20. Kim, S. K.; Bhatia, R.; Kim, T. H.; Seol, D.; Kim, J. H.; Kim, H.; Seung, W.; Kim, Y.; Lee, Y. H.; Kim, S. W., Directional dependent piezoelectric effect in CVD grown monolayer MoS2 for flexible piezoelectric nanogenerators. *Nano Energy* **2016,** *22*, 483-489.

21. Liu, X.; Yang, X.; Gao, G.; Yang, Z.; Liu, H.; Li, Q.; Lou, Z.; Shen, G.; Liao, L.; Pan, C.; Lin Wang, Z., Enhancing Photoresponsivity of Self-Aligned MoS2 Field-Effect Transistors by Piezo-Phototronic Effect from GaN Nanowires. *ACS Nano* **2016,** *10* (8), 7451-7.

22. Tu, D.; Xu, C. N.; Yoshida, A.; Fujihala, M.; Hirotsu, J.; Zheng, X. G., LiNbO3 :Pr(3+) : A Multipiezo Material with Simultaneous Piezoelectricity and Sensitive Piezoluminescence. *Adv. Mater.* **2017,** *29* (22).

23. Wu, W.; Wei, Y.; Wang, Z. L., Strain-gated piezotronic logic nanodevices. *Adv. Mater.* **2010,** *22* (42), 4711-5.

24. Yu, R.; Wu, W.; Pan, C.; Wang, Z.; Ding, Y.; Wang, Z. L., Piezo-phototronic Boolean Logic and Computation Using Photon and Strain Dual-Gated Nanowire Transistors. *Adv. Mater.* **2015,** *27* (5), 940-947.

25. Nie, J.; Hu, G.; Li, L.; Zhang, Y., Piezotronic analog-to-digital converters based on strain-gated transistors. *Nano Energy* **2018,** *46*, 423-427.

26. Zhu, L.; Wang, L.; Xue, F.; Chen, L.; Fu, J.; Feng, X.; Li, T.; Wang, Z. L., Piezo-Phototronic Effect Enhanced Flexible Solar Cells Based on n-ZnO/p-SnS Core-Shell Nanowire Array. *Adv Sci (Weinh)* **2017,** *4* (1), 1600185.

27. Zheng, D. Q.; Zhao, Z.; Huang, R.; Nie, J.; Li, L.; Zhang, Y., High-performance piezo-phototronic solar cell based on two-dimensional materials. *Nano Energy* **2017,** *32*, 448-453.

28. Wu, W.; Wen, X.; Wang, Z. L., Taxel-addressable matrix of vertical-nanowire piezotronic transistors for active and adaptive tactile imaging. *Science* **2013,** *340* (6135), 952-7.

29. Dan, M.; Hu, G.; Li, L.; Zhang, Y., High performance piezotronic logic nanodevices based on GaN/InN/GaN topological insulator. *Nano Energy* **2018,** *50*, 544-551.

30. Zhang, Y.; Hu, G.; Zhang, Y.; Li, L.; Willatzen, M.; Wang, Z. L., High performance piezotronic devices based on non-uniform strain. *Nano Energy* **2019,** *60*, 649-655.

31. Zhu, P.; Zhao, Z.; Nie, J.; Hu, G.; Li, L.; Zhang, Y., Ultra-high sensitivity strain sensor based on piezotronic bipolar transistor. *Nano Energy* **2018,** *50*, 744-749.

32. Zhou, J.; Gu, Y.; Fei, P.; Mai, W.; Gao, Y.; Yang, R.; Bao, G.; Wang, Z. L., Flexible piezotronic strain sensor. *Nano Lett.* **2008,** *8* (9), 3035-40.

33. Lai, Q.; Zhu, L.; Pang, Y.; Xu, L.; Chen, J.; Ren, Z.; Luo, J.; Wang, L.; Chen, L.; Han, K.; Lin, P.; Li, D.; Lin, S.; Chen, B.; Pan, C.; Wang, Z. L., Piezo-phototronic Effect Enhanced Photodetector Based on CH3NH3PbI3 Single Crystals. *ACS Nano* **2018,** *12* (10), 10501-10508.

34. Sun, J.; Hua, Q.; Zhou, R.; Li, D.; Guo, W.; Li, X.; Hu, G.; Shan, C.; Meng, Q.; Dong, L.; Pan, C.; Wang, Z. L., Piezo-phototronic Effect Enhanced Efficient Flexible Perovskite Solar Cells. *ACS Nano* **2019,** *13* (4), 4507-4513.

35. De Roo, J.; Ibanez, M.; Geiregat, P.; Nedelcu, G.; Walravens, W.; Maes, J.; Martins, J. C.; Van Driessche, I.; Kovalenko, M. V.; Hens, Z., Highly Dynamic Ligand Binding and Light

Absorption Coefficient of Cesium Lead Bromide Perovskite Nanocrystals. *ACS Nano* **2016,** *10* (2), 2071-81.

36. Lin, Q. Q.; Armin, A.; Nagiri, R. C. R.; Burn, P. L.; Meredith, P., Electro-optics of perovskite solar cells. *Nat. Photon.* **2015,** *9* (2), 106-112.

37. Turren-Cruz, S. H.; Saliba, M.; Mayer, M. T.; Juarez-Santiesteban, H.; Mathew, X.; Nienhaus, L.; Tress, W.; Erodici, M. P.; Sher, M. J.; Bawendi, M. G.; Gratzel, M.; Abate, A.; Hagfeldt, A.; Correa-Baena, J. P., Enhanced charge carrier mobility and lifetime suppress hysteresis and improve efficiency in planar perovskite solar cells. *Energy Environ. Sci.* **2018,** *11* (1), 78-86.

38. Slavney, A. H.; Hu, T.; Lindenberg, A. M.; Karunadasa, H. I., A Bismuth-Halide Double Perovskite with Long Carrier Recombination Lifetime for Photovoltaic Applications. *J. Am. Chem. Soc.* **2016,** *138* (7), 2138-41.

39. Dong, Q.; Fang, Y.; Shao, Y.; Mulligan, P.; Qiu, J.; Cao, L.; Huang, J., Solar cells. Electron-hole diffusion lengths > 175 mum in solution-grown CH3NH3PbI3 single crystals. *Science* **2015,** *347* (6225), 967-70.

40. Shi, D.; Adinolfi, V.; Comin, R.; Yuan, M.; Alarousu, E.; Buin, A.; Chen, Y.; Hoogland, S.; Rothenberger, A.; Katsiev, K.; Losovyj, Y.; Zhang, X.; Dowben, P. A.; Mohammed, O. F.; Sargent, E. H.; Bakr, O. M., Solar cells. Low trap-state density and long carrier diffusion in organolead trihalide perovskite single crystals. *Science* **2015,** *347* (6221), 519-22.

41. Leijtens, T.; Stranks, S. D.; Eperon, G. E.; Lindblad, R.; Johansson, E. M.; McPherson, I. J.; Rensmo, H.; Ball, J. M.; Lee, M. M.; Snaith, H. J., Electronic properties of meso-superstructured and planar organometal halide perovskite films: charge trapping, photodoping, and carrier mobility. *ACS Nano* **2014,** *8* (7), 7147-55.

42. Yettapu, G. R.; Talukdar, D.; Sarkar, S.; Swarnkar, A.; Nag, A.; Ghosh, P.; Mandal, P., Terahertz Conductivity within Colloidal CsPbBr3 Perovskite Nanocrystals: Remarkably High Carrier Mobilities and Large Diffusion Lengths. *Nano Lett.* **2016,** *16* (8), 4838-48.

43. You, Y. M.; Liao, W. Q.; Zhao, D.; Ye, H. Y.; Zhang, Y.; Zhou, Q.; Niu, X.; Wang, J.; Li, P. F.; Fu, D. W.; Wang, Z.; Gao, S.; Yang, K.; Liu, J. M.; Li, J.; Yan, Y.; Xiong, R. G., An organic-inorganic perovskite ferroelectric with large piezoelectric response. *Science* **2017,** *357* (6348), 306-309.

44. Dong, Q.; Song, J.; Fang, Y.; Shao, Y.; Ducharme, S.; Huang, J., Lateral-Structure Single-Crystal Hybrid Perovskite Solar Cells via Piezoelectric Poling. *Adv. Mater.* **2016,** *28* (14), 2816-21.

45. Coll, M.; Gomez, A.; Mas-Marza, E.; Almora, O.; Garcia-Belmonte, G.; Campoy-Quiles, M.; Bisquert, J., Polarization Switching and Light-Enhanced Piezoelectricity in Lead Halide Perovskites. *J Phys Chem Lett* **2015,** *6* (8), 1408-13.

46. Liao, W. Q.; Zhang, Y.; Hu, C. L.; Mao, J. G.; Ye, H. Y.; Li, P. F.; Huang, S. D.; Xiong, R. G., A lead-halide perovskite molecular ferroelectric semiconductor. *Nat Commun* **2015,** *6*, 7338.

47. Stroppa, A.; Quarti, C.; De Angelis, F.; Picozzi, S., Ferroelectric Polarization of CH3NH3PbI3: A Detailed Study Based on Density Functional Theory and Symmetry Mode Analysis. *J Phys Chem Lett* **2015,** *6* (12), 2223-31.

48. Burschka, J.; Pellet, N.; Moon, S. J.; Humphry-Baker, R.; Gao, P.; Nazeeruddin, M. K.; Gratzel, M., Sequential deposition as a route to high-performance perovskite-sensitized solar cells. *Nature* **2013,** *499* (7458), 316-9.

49. Jeon, N. J.; Noh, J. H.; Kim, Y. C.; Yang, W. S.; Ryu, S.; Seok, S. I., Solvent engineering for high-performance inorganic-organic hybrid perovskite solar cells. *Nat. Mater.* **2014,** *13* (9), 897-

903.

50. Kim, Y. C.; Kim, K. H.; Son, D. Y.; Jeong, D. N.; Seo, J. Y.; Choi, Y. S.; Han, I. T.; Lee, S. Y.; Park, N. G., Printable organometallic perovskite enables large-area, low-dose X-ray imaging. *Nature* **2017,** *550* (7674), 87-91.

51. Hwang, K.; Jung, Y. S.; Heo, Y. J.; Scholes, F. H.; Watkins, S. E.; Subbiah, J.; Jones, D. J.; Kim, D. Y.; Vak, D., Toward large scale roll-to-roll production of fully printed perovskite solar cells. *Adv. Mater.* **2015,** *27* (7), 1241-7.

52. Liu, Y.; Li, F.; Perumal Veeramalai, C.; Chen, W.; Guo, T.; Wu, C.; Kim, T. W., Inkjet-Printed Photodetector Arrays Based on Hybrid Perovskite CH3NH3PbI3 Microwires. *ACS Appl Mater Interfaces* **2017,** *9* (13), 11662-11668.

53. Hu, W.; Huang, W.; Yang, S.; Wang, X.; Jiang, Z.; Zhu, X.; Zhou, H.; Liu, H.; Zhang, Q.; Zhuang, X.; Yang, J.; Kim, D. H.; Pan, A., High-Performance Flexible Photodetectors based on High-Quality Perovskite Thin Films by a Vapor-Solution Method. *Adv. Mater.* **2017,** *29* (43), 1703256.

54. Saidaminov, M. I.; Haque, M. A.; Savoie, M.; Abdelhady, A. L.; Cho, N.; Dursun, I.; Buttner, U.; Alarousu, E.; Wu, T.; Bakr, O. M., Perovskite Photodetectors Operating in Both Narrowband and Broadband Regimes. *Adv. Mater.* **2016,** *28* (37), 8144-8149.

55. Dou, L.; Yang, Y. M.; You, J.; Hong, Z.; Chang, W. H.; Li, G.; Yang, Y., Solution-processed hybrid perovskite photodetectors with high detectivity. *Nat Commun* **2014,** *5*, 5404.

56. García de Arquer, F. P.; Armin, A.; Meredith, P.; Sargent, E. H., Solution-processed semiconductors for next-generation photodetectors. *Nature Reviews Materials* **2017,** *2* (3).

57. Deng, W.; Zhang, X.; Huang, L.; Xu, X.; Wang, L.; Wang, J.; Shang, Q.; Lee, S. T.; Jie, J., Aligned Single-Crystalline Perovskite Microwire Arrays for High-Performance Flexible Image Sensors with Long-Term Stability. *Adv. Mater.* **2016,** *28* (11), 2201-8.

58. Bao, C.; Yang, J.; Bai, S.; Xu, W.; Yan, Z.; Xu, Q.; Liu, J.; Zhang, W.; Gao, F., High Performance and Stable All-Inorganic Metal Halide Perovskite-Based Photodetectors for Optical Communication Applications. *Adv. Mater.* **2018,** *30* (38), e1803422.

59. Fang, Y.; Dong, Q.; Shao, Y.; Yuan, Y.; Huang, J., Highly narrowband perovskite single-crystal photodetectors enabled by surface-charge recombination. *Nat. Photon.* **2015,** *9* (10), 679-686.

60. Dai, X.; Zhang, S.; Wang, Z.; Adamo, G.; Liu, H.; Huang, Y.; Couteau, C.; Soci, C., GaAs/AlGaAs nanowire photodetector. *Nano Lett.* **2014,** *14* (5), 2688-93.

61. Waleed, A.; Tavakoli, M. M.; Gu, L.; Wang, Z.; Zhang, D.; Manikandan, A.; Zhang, Q.; Zhang, R.; Chueh, Y. L.; Fan, Z., Lead-Free Perovskite Nanowire Array Photodetectors with Drastically Improved Stability in Nanoengineering Templates. *Nano Lett.* **2017,** *17* (1), 523-530.

62. Sahli, F.; Werner, J.; Kamino, B. A.; Brauninger, M.; Monnard, R.; Paviet-Salomon, B.; Barraud, L.; Ding, L.; Diaz Leon, J. J.; Sacchetto, D.; Cattaneo, G.; Despeisse, M.; Boccard, M.; Nicolay, S.; Jeangros, Q.; Niesen, B.; Ballif, C., Fully textured monolithic perovskite/silicon tandem solar cells with 25.2% power conversion efficiency. *Nat. Mater.* **2018,** *17* (9), 820-826.

63. Mei, A.; Li, X.; Liu, L.; Ku, Z.; Liu, T.; Rong, Y.; Xu, M.; Hu, M.; Chen, J.; Yang, Y.; Gratzel, M.; Han, H., A hole-conductor-free, fully printable mesoscopic perovskite solar cell with high stability. *Science* **2014,** *345* (6194), 295-8.

64. Tung, R. T., Recent advances in Schottky barrier concepts. *Materials Science & Engineering R-Reports* **2001,** *35* (1-3), 1-138.

65. Tersoff, J., Schottky Barrier Heights and the Continuum of Gap States. *Phys. Rev. Lett.* **1984,** *52* (6), 465-468.

66. Jeon, N. J.; Noh, J. H.; Yang, W. S.; Kim, Y. C.; Ryu, S.; Seo, J.; Seok, S. I., Compositional engineering of perovskite materials for high-performance solar cells. *Nature* **2015,** *517* (7535), 476-80.

67. Dualeh, A.; Tétreault, N.; Moehl, T.; Gao, P.; Nazeeruddin, M. K.; Grätzel, M., Effect of Annealing Temperature on Film Morphology of Organic-Inorganic Hybrid Pervoskite Solid-State Solar Cells. *Adv. Funct. Mater.* **2014,** *24* (21), 3250-3258.

68. Pesquera, D.; Herranz, G.; Barla, A.; Pellegrin, E.; Bondino, F.; Magnano, E.; Sanchez, F.; Fontcuberta, J., Surface symmetry-breaking and strain effects on orbital occupancy in transition metal perovskite epitaxial films. *Nat Commun* **2012,** *3*, 1189.

69. Laukhin, V.; Copie, O.; Rozenberg, M. J.; Weht, R.; Bouzehouane, K.; Reyren, N.; Jacquet, E.; Bibes, M.; Barthelemy, A.; Herranz, G., Electronic subband reconfiguration in a d0-perovskite induced by strain-driven structural transformations. *Phys. Rev. Lett.* **2012,** *109* (22), 226601.

70. Choi, K. J.; Biegalski, M.; Li, Y. L.; Sharan, A.; Schubert, J.; Uecker, R.; Reiche, P.; Chen, Y. B.; Pan, X. Q.; Gopalan, V.; Chen, L. Q.; Schlom, D. G.; Eom, C. B., Enhancement of ferroelectricity in strained BaTiO3 thin films. *Science* **2004,** *306* (5698), 1005-9.

71. Matthews, J. W.; Blakeslee, A. E., Defects in epitaxial multilayers. *J. Cryst. Growth* **1974,** *27*, 118-125.

72. Herklotz, A.; Lee, D.; Guo, E. J.; Meyer, T. L.; Petrie, J. R.; Lee, H. N., Strain coupling of oxygen non-stoichiometry in perovskite thin films. *J Phys Condens Matter* **2017,** *29* (49), 493001.

73. Stoerzinger, K. A.; Choi, W. S.; Jeen, H.; Lee, H. N.; Shao-Horn, Y., Role of Strain and Conductivity in Oxygen Electrocatalysis on LaCoO3 Thin Films. *J Phys Chem Lett* **2015,** *6* (3), 487-92.

74. Pan, C.; Dong, L.; Zhu, G.; Niu, S.; Yu, R.; Yang, Q.; Liu, Y.; Wang, Z. L., High-resolution electroluminescent imaging of pressure distribution using a piezoelectric nanowire LED array. *Nat. Photon.* **2013,** *7* (9), 752-758.

75. Peng, M.; Li, Z.; Liu, C.; Zheng, Q.; Shi, X.; Song, M.; Zhang, Y.; Du, S.; Zhai, J.; Wang, Z. L., High-resolution dynamic pressure sensor array based on piezo-phototronic effect tuned photoluminescence imaging. *ACS Nano* **2015,** *9* (3), 3143-50.

76. Chen, M.; Zhao, B.; Hu, G.; Fang, X.; Wang, H.; Wang, L.; Luo, J.; Han, X.; Wang, X.; Pan, C.; Wang, Z. L., Piezo-Phototronic Effect Modulated Deep UV Photodetector Based on ZnO-Ga2O3 Heterojuction Microwire. *Adv. Funct. Mater.* **2018,** *28* (14).

Figure captions

Figure 1. Experiment Schematic of the MAPbI$_3$ photodetector. (a) PbI$_2$ and MAI in DMF solution with ratio 1:1. (b) Solution spin coating of MAPbI$_3$. (c) Annealing process of perovskite film at 100 ℃. (d) Electrodes array deposition process using a metal mask. (e) Experimental setup for I-V measurement of the perovskite film. (f) Strain generator and strain calculation methods.

Figure 2. Characterization of perovskite polycrystals. (a) Schematic of the tetragonal and orthorhombic CH$_3$NH$_3$PbI$_3$ perovskite, (b) XRD spectrum of MAPbI$_3$ thin film, (c) SEM top-view image and cross-sectional image of MAPbI$_3$ layers, (d) absorption spectra of MAPbI$_3$ perovskite film.

Figure 3. Properties of MAPbI$_3$ perovskites in negative polarization charges case (a) I-V characteristics with different strains with illumination power density valued 31.7 µW/cm^2. (b) I-V characteristics with different illumination power density with 1.4% strain. (c) Current versus illumination power density under various strains. (d) I- ε curves with different illumination power densities.

Figure 4. Principle of MAPbI$_3$ perovskite photodetectors (a) Vertical structure of perovskite detector. (b) Electric field distribution of the device under the voltage and strain. (c) change of the band structure near the metal-semiconductor contact in MAPbI$_3$ crystal under electric field, strain, and light. (d) The opposite trend to (c). (e) An increase in the Schottky barrier, due to the movement of polarized charge carriers. (f) A decrease in the Schottky barrier, due to the opposite movement direction of polarized charge carriers to the electric field.

Figure 5. Properties of MAPbI$_3$ perovskites in positive polarization charges case (a) I-V characteristics with different strains with illumination power density valued at 6.6 µW/cm^2. (b) A positive effect of photocurrent on strain with different voltages at 6.6 µW/cm^2 illumination power density (c) I-V characteristics of another type of device (D2) with different strains with illumination power density valued at 6.6 µW/cm^2. (d) I- ε curves with different voltage at 6.6 µW/cm^2 illumination power density for device type D2.

Figure 6. R, Photoresponsivity and its relative value change induced by strain in the negative and positive polarization charges case (a) R, Photoresponsivity and $\Delta R/R$, relative change (c) of photoresponsivity of the device with various bias in the positive polarization charges case. (b) R, Photoresponsivity and $\Delta R/R$, relative change (d) of photoresponsivity of the device with various bias in the negative polarization charges case.

Figure 7. Transient response of the photodetector under 10 V bias voltage. Response time under different strain in the positive (a) and negative (b) polarization charges case. Response time changes with strain in in the positive (c) and negative (d) polarization charges case.

(a) PbI$_2$ MAI

(b)

(c) Heating

(d) Au
Metal mask

(e) Microscope
Keithley 4200

(f) d
θ
L
$\varepsilon = \dfrac{d \times sin\theta}{L} \times 100\%$
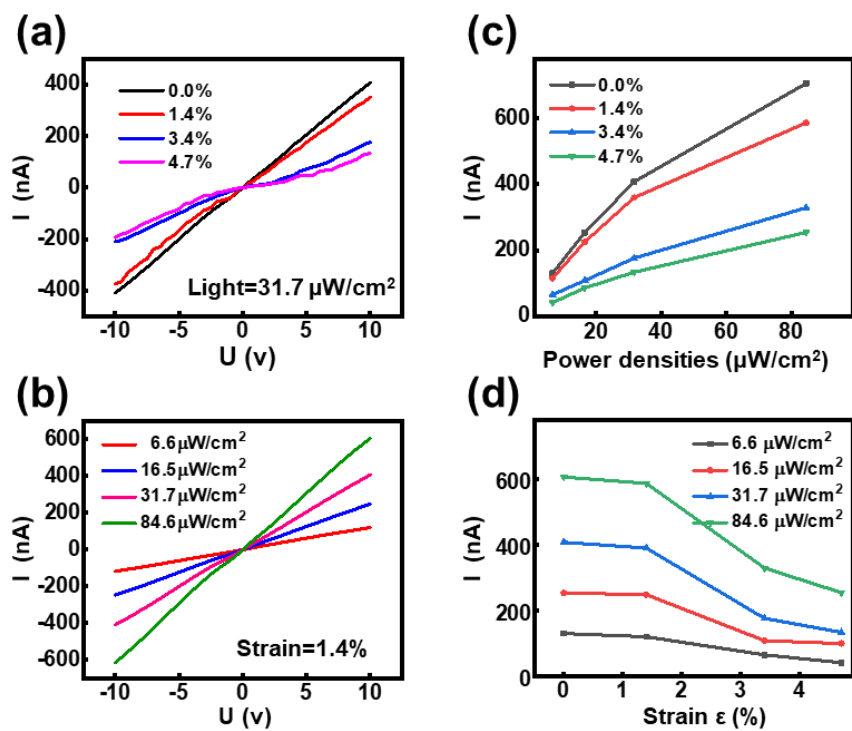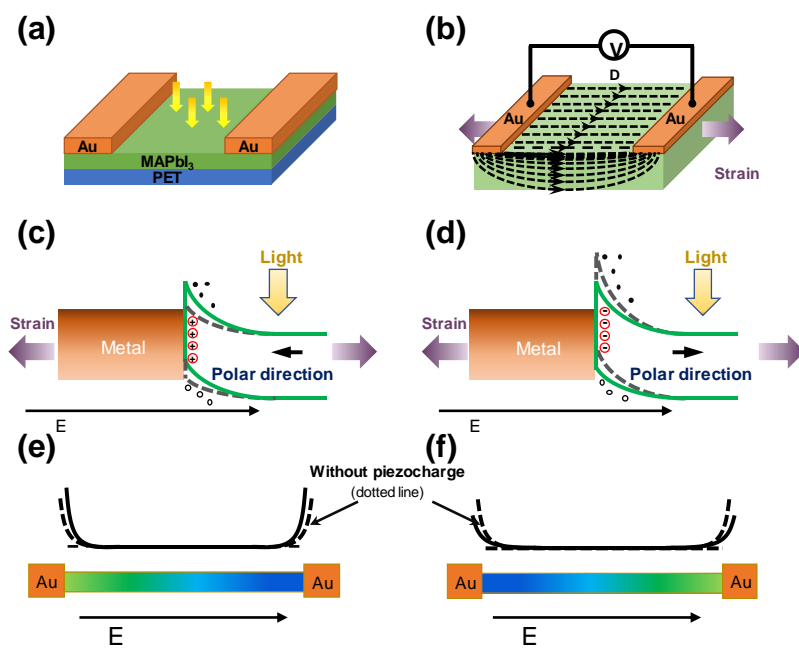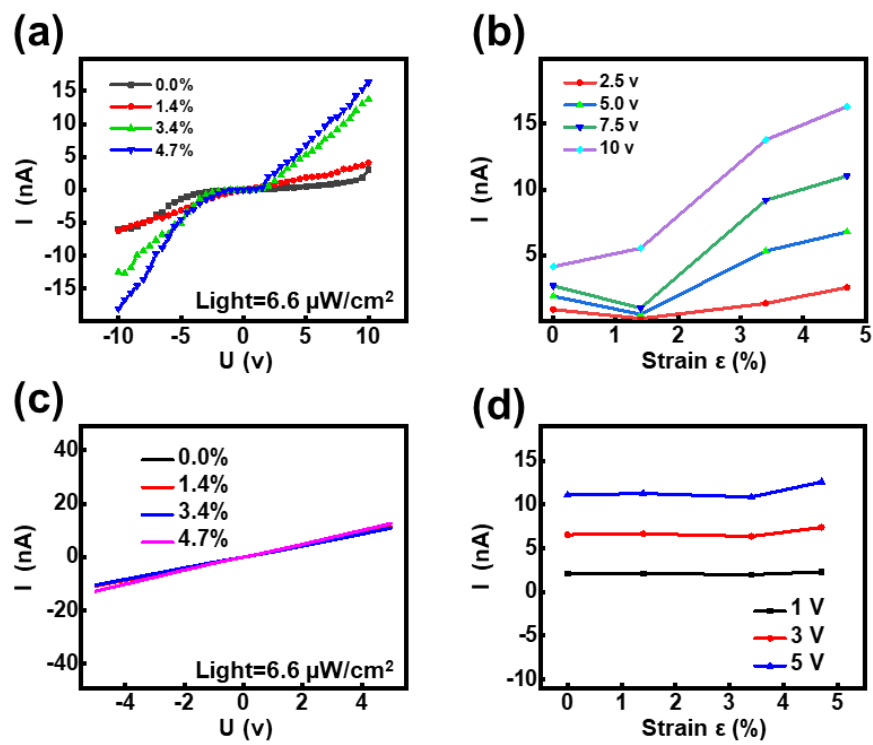
Figure 1

(a)

H
N
C
Pb
I

(b)

(c)

1 μm

(d)

Absorption
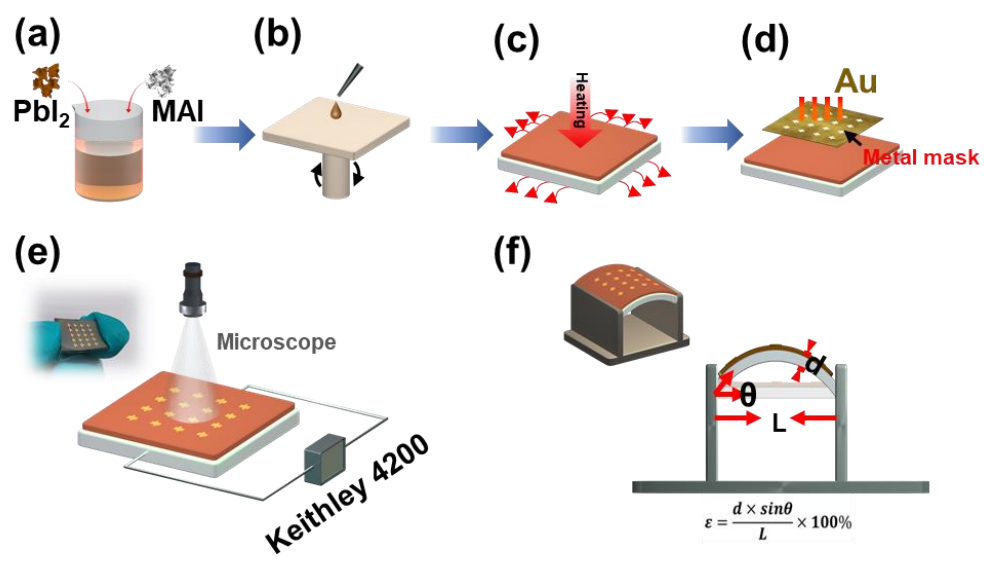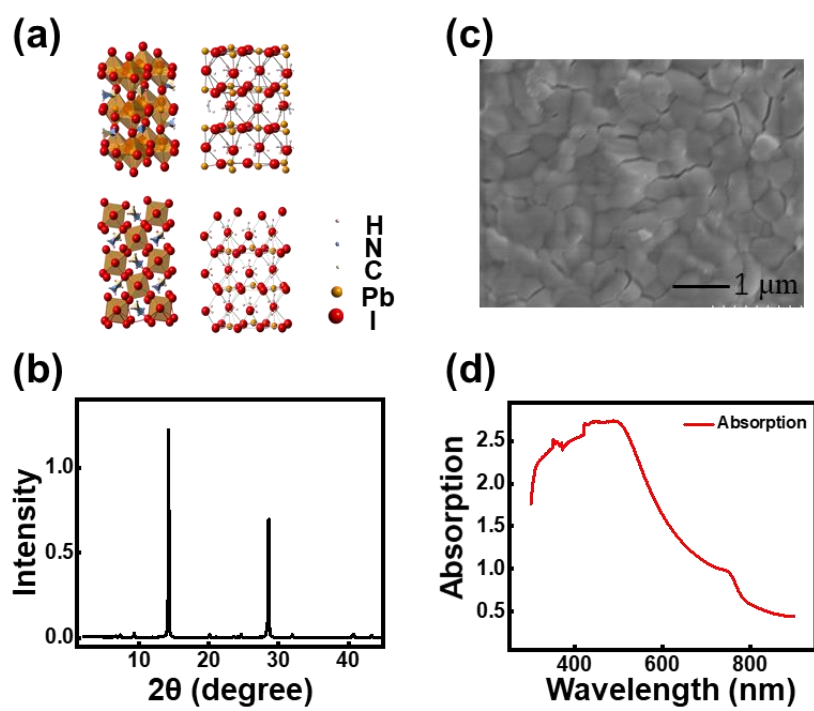
Figure 2

Figure 3

Figure 4

Figure 5

Figure 6

Figure 7